



BNL-209465-2018-JAAM

# Deconvolution of octahedral Pt<sub>3</sub>Ni nanoparticle growth pathway from in situ characterizations

X. Shen, I. Waluyo

To be published in "NATURE COMMUNICATIONS"

October 2018

Photon Sciences

**Brookhaven National Laboratory**

**U.S. Department of Energy**

USDOE Office of Science (SC), Basic Energy Sciences (BES) (SC-22)

Notice: This manuscript has been authored by employees of Brookhaven Science Associates, LLC under Contract No. DE-SC0012704 with the U.S. Department of Energy. The publisher by accepting the manuscript for publication acknowledges that the United States Government retains a non-exclusive, paid-up, irrevocable, world-wide license to publish or reproduce the published form of this manuscript, or allow others to do so, for United States Government purposes.

## **DISCLAIMER**

This report was prepared as an account of work sponsored by an agency of the United States Government. Neither the United States Government nor any agency thereof, nor any of their employees, nor any of their contractors, subcontractors, or their employees, makes any warranty, express or implied, or assumes any legal liability or responsibility for the accuracy, completeness, or any third party's use or the results of such use of any information, apparatus, product, or process disclosed, or represents that its use would not infringe privately owned rights. Reference herein to any specific commercial product, process, or service by trade name, trademark, manufacturer, or otherwise, does not necessarily constitute or imply its endorsement, recommendation, or favoring by the United States Government or any agency thereof or its contractors or subcontractors. The views and opinions of authors expressed herein do not necessarily state or reflect those of the United States Government or any agency thereof.

1 **Title: Deconvolution of octahedral Pt<sub>3</sub>Ni nanoparticle growth pathway from *in***  
2 ***situ* characterizations**

3 **Authors:** Xiaochen Shen<sup>1,‡</sup>, Changlin Zhang<sup>1,‡</sup>, Shuyi Zhang<sup>2,3,‡</sup>, Sheng Dai<sup>2,3,‡</sup>, Guanghui  
4 Zhang<sup>5,‡</sup>, Mingyuan Ge<sup>6,‡</sup>, Yanbo Pan<sup>1</sup>, Stephen M. Sharkey<sup>1</sup>, George W. Graham<sup>2,3</sup>, Adrian  
5 Hunt<sup>6</sup>, Iradwikanari Waluyo<sup>6,\*</sup>, Jeffrey T. Miller<sup>5,\*</sup>, Xiaoqing Pan<sup>3,4,\*</sup>, Zhenmeng Peng<sup>1,\*</sup>

6 **Affiliations:**

7 <sup>1</sup> Department of Chemical and Biomolecular Engineering, The University of Akron, Akron, Ohio  
8 44325, United States.

9 <sup>2</sup> Department of Materials Science and Engineering, University of Michigan, Ann Arbor,  
10 Michigan 48109, United States.

11 <sup>3</sup> Department of Chemical Engineering and Materials Science, University of California-Irvine,  
12 Irvine, California 92697, United States.

13 <sup>4</sup> Department of Physics and Astronomy, University of California-Irvine, Irvine, California,  
14 92697, United States

15 <sup>5</sup> Davidson School of Chemical Engineering, Purdue University, West Lafayette, Indiana 47907,  
16 United States

17 <sup>6</sup> National Synchrotron Light Source II, Brookhaven National Laboratory, Upton, New York  
18 11973, United States

19 \*Correspondence to: [zpeng@uakron.edu](mailto:zpeng@uakron.edu), [xiaoqinpan@uci.edu](mailto:xiaoqinpan@uci.edu), [jeffrey-t-miller@purdue.edu](mailto:jeffrey-t-miller@purdue.edu),  
20 [iwaluyo@bnl.gov](mailto:iwaluyo@bnl.gov).

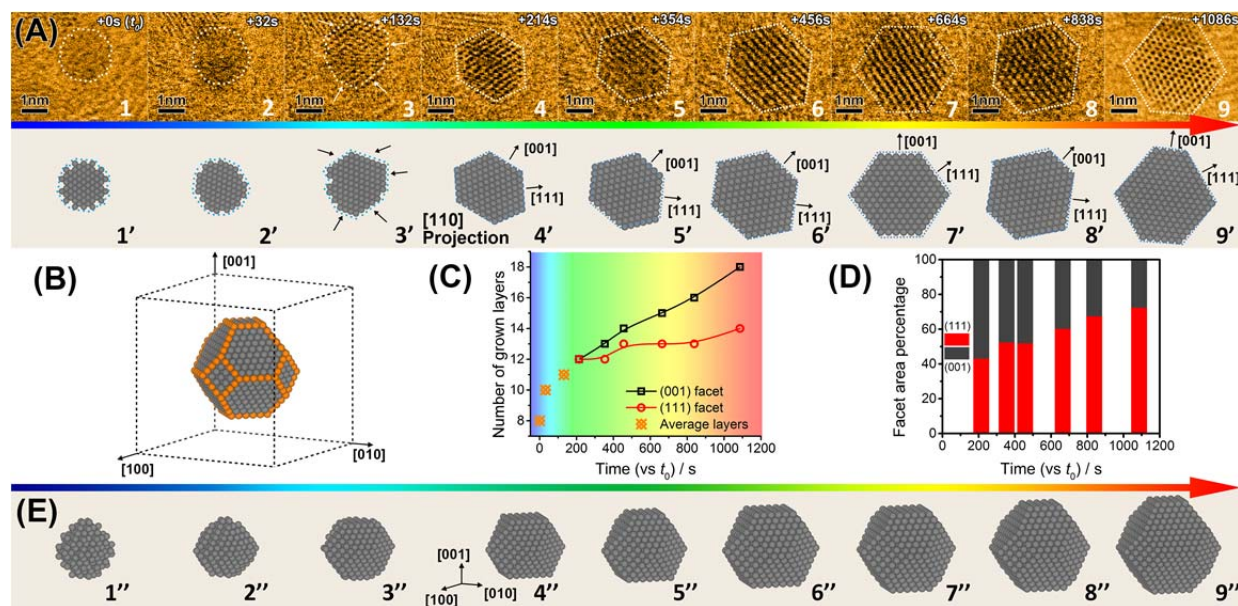
21 ‡These authors contributed equally.

22 **Abstract:** Understanding the growth pathway of faceted alloy nanoparticles at the atomic level is  
23 crucial to morphology control and property tuning. Yet, it remains a challenge due to complexity  
24 of the growth process and technical limits of modern characterization tools. We report a  
25 combinational use of multiple cutting-edge *in situ* techniques to study the growth process of  
26 octahedral Pt<sub>3</sub>Ni nanoparticles, which reveal the particle growth and facet formation  
27 mechanisms. Our studies confirm the formation of octahedral Pt<sub>3</sub>Ni initiates from Pt nuclei  
28 generation, which is followed by continuous Pt reduction that simultaneously catalyzes Ni  
29 reduction, resulting in mixed alloy formation with moderate elemental segregation. Carbon  
30 monoxide molecules serve as a facet formation modulator and induce Ni segregation to the  
31 surface, which inhibits the (111) facet growth and causes the particle shape to evolve from a  
32 spherical cluster to an octahedron as the (001) facet continues to grow.

33  
34 **Main Text:** Faceted platinum alloy nanoparticles, in particular octahedral Pt-Ni, have been  
35 recognized as one of the most promising cathode catalysts for use in hydrogen fuel cells for their  
36 dramatically improved oxygen reduction reaction (ORR) activity compared to their spherical  
37 counterparts and pure Pt<sup>1-4</sup>. These findings revealed significant catalytic structure-property  
38 correlations and suggested the importance of controlling the facet growth of nanoparticles to  
39 achieve the desired property. Although considerable success has been achieved in synthesizing

40 faceted alloy nanoparticles after years of intensive research, these achievements were mostly  
 41 empirical. A good knowledge of the growth pathway, which is essential to guide rational  
 42 synthesis, is still lacking. The past decade has witnessed technological advances of *in situ*  
 43 electron microscopy and its uses in obtaining the growth trajectory of pure metal nanoparticles<sup>5-</sup>  
 44<sup>12</sup>. Compared with pure metals, the growth pathway of faceted alloy nanoparticles is more  
 45 complicated. With multiple elements being involved, it is challenging to identify their behaviors,  
 46 both individually as different elements and collectively as alloy components, during the particle  
 47 growth<sup>13, 14</sup>.

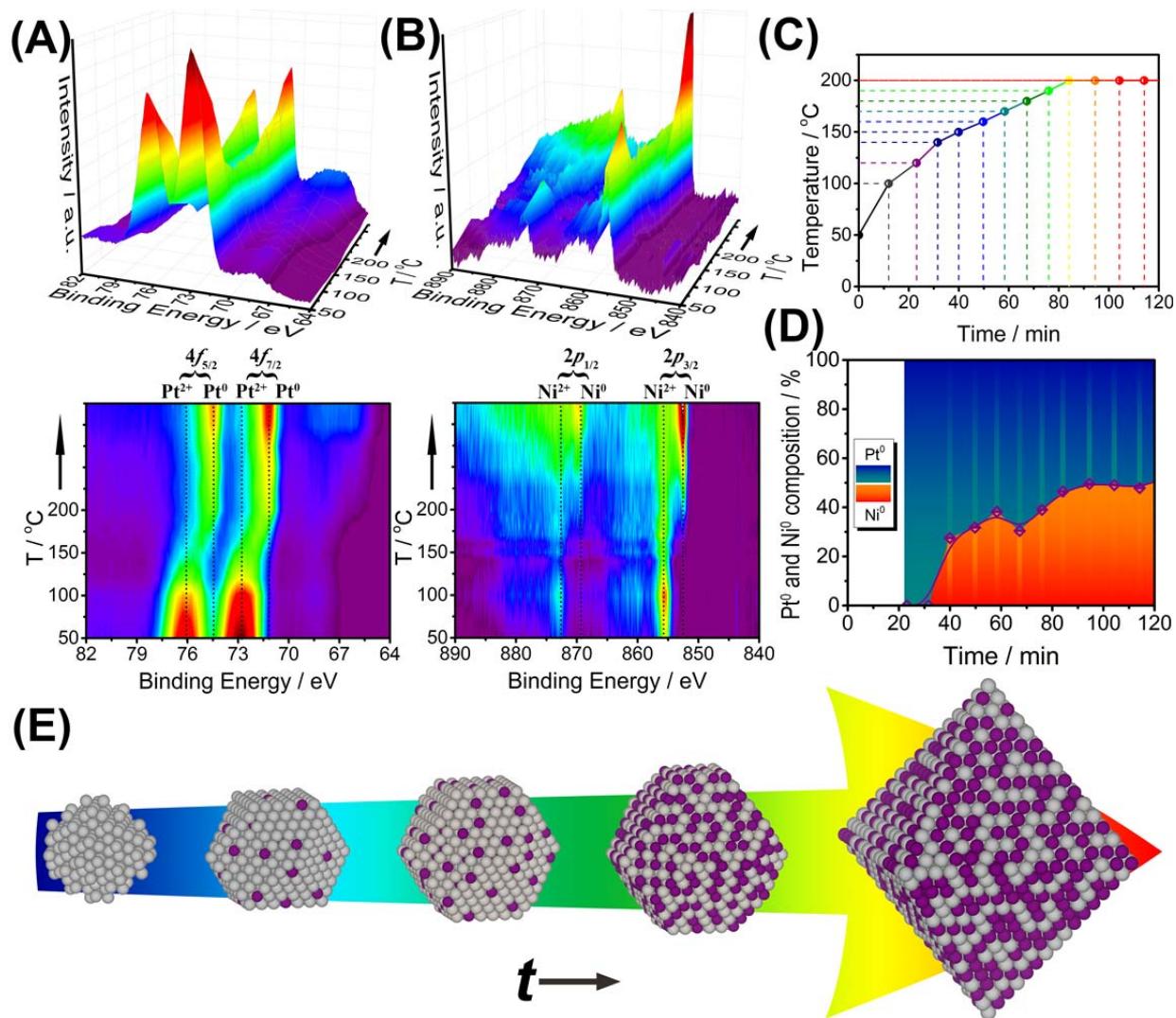
48 Herein we report a combinational use of several cutting-edge *in situ* characterization techniques,  
 49 including aberration-corrected scanning transmission electron microscopy (AC-STEM), ambient  
 50 pressure X-ray photoelectron spectroscopy (AP-XPS) and X-ray absorption spectroscopy (XAS),  
 51 to study the growth process of octahedral Pt<sub>3</sub>Ni nanoparticles. By integrating the information  
 52 obtained from these techniques, together with computational simulations, a clear pathway for the  
 53 particle growth and facet formation is revealed.



54  
 55 **Fig. 1.** (A) *In situ* STEM images of one growing Pt<sub>3</sub>Ni nanoparticle (upper row) and  
 56 corresponding 2D projection model (lower row), (B) Representative atomic model (not to scale)  
 57 of the nanoparticle during growth, (C) Number of grown layers of the (001) and (111) facets and  
 58 (D) their surface exposure ratio as function of experimental time, (E) 3D model (not to scale)  
 59 of the Pt<sub>3</sub>Ni growth process.

60  
 61 Direct visualization of the growth process of octahedral Pt<sub>3</sub>Ni was performed on a JEOL-JEM  
 62 3100R05 microscope that is equipped with a Protochips Atmosphere<sup>TM</sup> gas cell system (fig. S1)  
 63<sup>15, 16</sup>, realizing dynamic observation at the atomic scale under atmospheric pressures. The  
 64 reaction condition for growing octahedral Pt<sub>3</sub>Ni followed one solid-state chemistry method we  
 65 recently developed, in which H<sub>2</sub> acts as a reductant and CO acts as a capping agent for  
 66 morphology control<sup>1</sup>. Fig. 1(A) shows the time-sequenced STEM images of one single particle  
 67 at its different growth stages (top row). Simulated images, presented in the bottom row, were

68 obtained based on the experimental data. It was challenging to image the particles clearly at their  
69 early growth stage (denoted as  $t_0 = 0$  s), primarily because of their structural instability and  
70 mobility in the cluster size range. Moreover, the use of low-dose STEM imaging condition,  
71 which was necessary for minimizing the electron beam effect, sacrificed the image quality to  
72 some extent (see more discussions in supplementary materials, fig. S4). Nevertheless, the sphere-  
73 like characteristic indicated no apparent facet formation of the particles in their early growth  
74 stage. Facet formation and distinct lattice fringes were observed to evolve when the particle size  
75 slightly exceeded 1 nm. Two groups of facets, i.e.  $\{111\}$  and  $\{001\}$ , were indexed. Noticeably,  
76 the  $\{111\}$  facets exhibited a significantly slower growth rate compared with the  $\{001\}$  under the  
77 reaction condition, which was evidenced by a smaller number of atomic layers along the  $[111]$   
78 axis than along the  $[001]$  (Fig. 1(C)). Our previous study has identified the important role of CO  
79 molecules in inhibiting the  $\text{Pt}_3\text{Ni}$   $\{111\}$  growth<sup>1</sup>, which led to the formation of octahedral  
80 morphology rather than a spheroid one. The slower  $\{111\}$  growth resulted in the gradual  
81 domination of this group of facet planes and diminishment of the  $\{001\}$  over the reaction time  
82 (Fig. 1(D), S6), which was accompanied by a continuous morphological change of the growing  
83 particle. The *in situ* observation of other individual particles showed the same trend (fig. S7 and  
84 S8), suggesting a generic pathway for their growth. We constructed three-dimensional (3D)  
85 models based on the *in situ* STEM data to better illustrate the whole growth process of octahedral  
86  $\text{Pt}_3\text{Ni}$  (Fig. 1(E)), in which it experienced a continual increase in size along with a gradual  
87 morphological transition from spherical cluster to polyhedron and finally to octahedron.



88

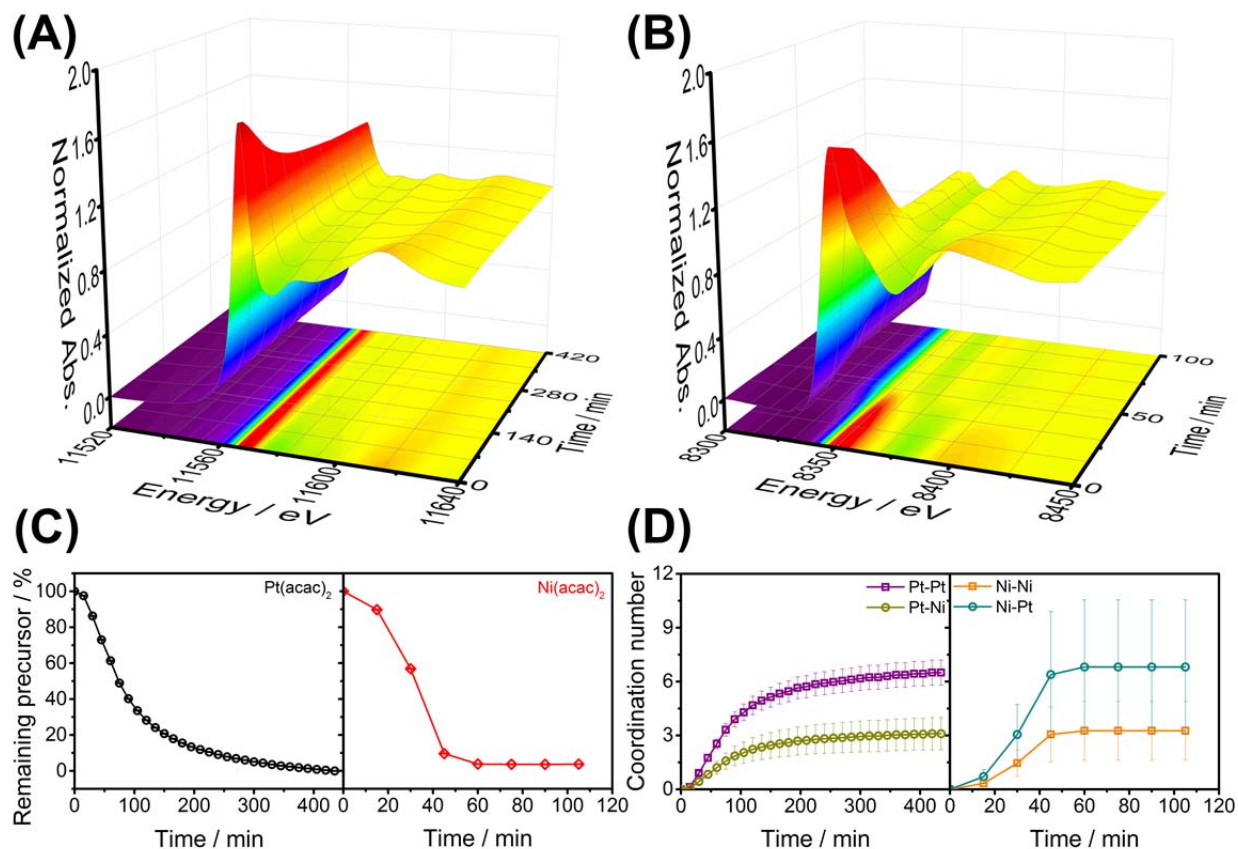
89 **Fig. 2.** (A) Pt 4f and (B) Ni 2p AP-XPS spectra and corresponding 2D projections of growing  
 90 particles, (C) Temperature profile as a function of experiment time, (D) Calculated Pt<sup>0</sup> and Ni<sup>0</sup>  
 91 contents near surface region of the growing particles based on quantitative XPS analyses, (E)  
 92 Growth model (not to scale) of Pt<sub>3</sub>Ni nanoparticle with near surface Pt<sup>0</sup>/Ni<sup>0</sup> ratio changes (gray:  
 93 Pt; purple: Ni).

94

95 *In situ* AP-XPS experiments were conducted to characterize the elemental distribution near the  
 96 particle surface region through the growth process by continuously collecting Pt 4f and Ni 2p  
 97 signals under the synthesis condition (see experimental details in the supplementary materials).  
 98 Fig. 2(A) and 2(B) show the original Pt 4f and Ni 2p spectra collected according to the  
 99 temperature profile in Fig. 2(C). Peaks at 72.8 and 76.1 eV, corresponding to Pt<sup>2+</sup> 4f<sub>7/2</sub> and 4f<sub>5/2</sub>  
 100 <sup>17</sup>, and peaks at 855.7 and 873.1 eV, corresponding to Ni<sup>2+</sup> 2p<sub>3/2</sub> and 2p<sub>1/2</sub> <sup>18</sup>, were identified prior  
 101 to the experiments, indicating that both elements remained in their precursor state. A new peak  
 102 emerged at 71.7 eV when the temperature was raised to around 120 °C. This new peak was  
 103 assigned to Pt<sup>0</sup> 4f<sub>7/2</sub>, with its emergence suggesting an initiation of Pt reduction. Gradual growth

104 of the Pt<sup>0</sup> 4f<sub>7/2</sub> peak and diminishment of the Pt<sup>2+</sup> 4f<sub>7/2</sub> peak were observed with a further increase  
105 in the temperature, which indicated a continual Pt reduction process. Ni exhibited a delayed  
106 reduction compared to Pt, because the Ni<sup>0</sup> 2p<sub>3/2</sub> peak at 852.7 eV did not appear until the  
107 temperature was above 150 °C. Control experiments were conducted with pure Pt(acac)<sub>2</sub> and  
108 Ni(acac)<sub>2</sub> to characterize their individual reduction processes (fig. S9 and S10). The onset  
109 reduction temperature for Pt(acac)<sub>2</sub> remained at around 120 °C, whereas Ni(acac)<sub>2</sub> cannot be  
110 effectively reduced until above 200 °C. This interesting observation suggested that reduced Pt  
111 served as a catalyst for Ni reduction.

112 Quantitative analyses of the AP-XPS data set (see more discussions in supplementary materials)  
113 yielded more detailed composition information of the growing particles in their near surface  
114 region (Fig. 2(D)), which provided an important basis for understanding the particle growth  
115 pathway. Because Pt reduction initiated at around 120 °C and no metallic Ni was detected until  
116 150 °C, it could be concluded that Pt, rather than a Pt-Ni alloy, constituted the particles at their  
117 nucleation and early growth stage and served as seeds for the octahedral Pt<sub>3</sub>Ni formation. Above  
118 150 °C, Ni began to be effectively reduced, as evidenced by a rapid increase in the Ni<sup>0</sup> content.  
119 In addition, a gradual shift of Pt<sup>0</sup> 4f<sub>7/2</sub> peak from 71.7 to 71.2 eV was observed in this stage (Fig.  
120 2(A)), which can be attributed to electron transfer from Ni<sup>0</sup> to Pt<sup>0</sup> and was consistent with the  
121 quantitative surface composition change<sup>19</sup>. Interestingly, the near surface Ni<sup>0</sup> content gradually  
122 reached nearly 50 at% at the late particle growth stage, which was significantly higher than its  
123 average content of 25 at% in the final Pt<sub>3</sub>Ni product. This discrepancy suggested the grown  
124 particles were Ni-enriched in the surface region, which was in good agreement with previous  
125 studies in literature<sup>20</sup>. Another interesting observation was that the surface Ni content, despite of  
126 its higher onset reduction temperature than Pt, reached 25 at% soon after its reduction and  
127 remained above this value until completion of the reduction process. It revealed, besides Ni  
128 reduction, that Ni in the bulk likely underwent a continual segregation to the surface region  
129 during the particle growth process. By combining the information obtained from STEM and AP-  
130 XPS, we were able to depict both morphological and surface composition changes of the  
131 growing particles. As illustrated in Fig. 2(E), the growth of octahedral Pt<sub>3</sub>Ni starts with the  
132 formation of Pt nuclei and small spherical clusters, which continues to evolve through  
133 polyhedron to octahedron in morphology and evolve from pure Pt to about Pt<sub>50</sub>Ni<sub>50</sub> in surface  
134 composition.



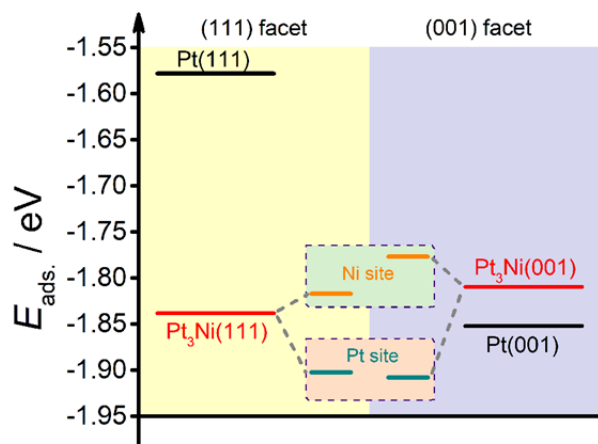
135

136 **Fig. 3.** (A) Pt L<sub>3</sub>-edge and (B) Ni K-edge XAS spectra of the growing nanoparticles, (C)  
 137 percentage of remaining precursors calculated from the XAS data and (D) Coordination numbers  
 138 of the reduced elements calculated from the XAS data as function of reaction time.

139

140 *In situ* XAS experiments were carried out to trace overall composition changes of the growing  
 141 particles<sup>21,22</sup>. Note that the experiments were conducted at a relatively lower temperature of 160  
 142 °C compared to that in AC-STEM and AP-XPS experiments so that the particle growth kinetics  
 143 was sufficiently slow to allow for *in situ* XAS measurements, given that it took approximately 15  
 144 minutes to collect one XAS spectrum (see supplementary materials for experimental details).  
 145 Our control experiments confirmed that such a change in reaction temperature altered the particle  
 146 growth kinetics but would not affect the grown particle morphology and composition (fig. S11  
 147 and S12), which validated a combinational use of the *in situ* XAS data. Pt L<sub>3</sub>-edge and Ni K-  
 148 edge spectra were collected in time series during the particle growth process (Fig. 3(A), 3(B) and  
 149 fig. S12). The extents of Pt and Ni reduction were evaluated based on changes in their XANES  
 150 spectra. Fig. 3(C) shows the plot of the percentage of remaining precursors at different reaction  
 151 time. It was apparent that Ni reduction occurred more rapidly than Pt once it was initiated, as  
 152 shown by a shorter period of time before the precursor depletion. The control XAS experiments  
 153 with Ni(acac)<sub>2</sub> showed little Ni reduction by itself under the same experimental condition (fig.  
 154 S13). The results were in good agreement with the AP-XPS findings, which further supported  
 155 our conclusion that Ni reduction was catalyzed by Pt. The completion of Ni reduction in a  
 156 shorter time than that for Pt could lead to an argument that the grown particles should have Pt-

157 enriched surfaces, which contradicted the AP-XPS observation of Ni enrichment in the surfaces.  
 158 This contradiction can be resolved on the basis of Ni segregation to the surface during the  
 159 octahedral Pt<sub>3</sub>Ni growth, as revealed by the AP-XPS data. This explanation was supported by  
 160 post-treatment experiments with octahedral Pt<sub>3</sub>Ni in previous studies, which reported significant  
 161 surface Ni segregation upon particle exposure to CO atmosphere<sup>23</sup>. Average coordination  
 162 numbers for reduced Pt and Ni during the particle growth were calculated from the XAS data  
 163 (Fig 3(D)). The Pt-Pt coordination number remained higher than that of Pt-Ni throughout the  
 164 reaction, with the ratio gradually increasing with time. In comparison, the Ni-Pt coordination  
 165 number was higher than that of Ni-Ni coordination and their ratio seemed stabilized after the  
 166 completion of the Ni reduction. The values of both ratios (Pt-Pt/Pt-Ni and Ni-Pt/Ni-Ni) in the  
 167 grown octahedral Pt<sub>3</sub>Ni deviated from the Pt/Ni atomic ratio (i.e. 3:1) to a moderate extent.  
 168 Considering the Pt enrichment in core region of the grown particles also contributed to such  
 169 deviations, the results indicated that although Ni atoms were enriched on the surface, they were  
 170 relatively well mixed with Pt atoms in the lattice.



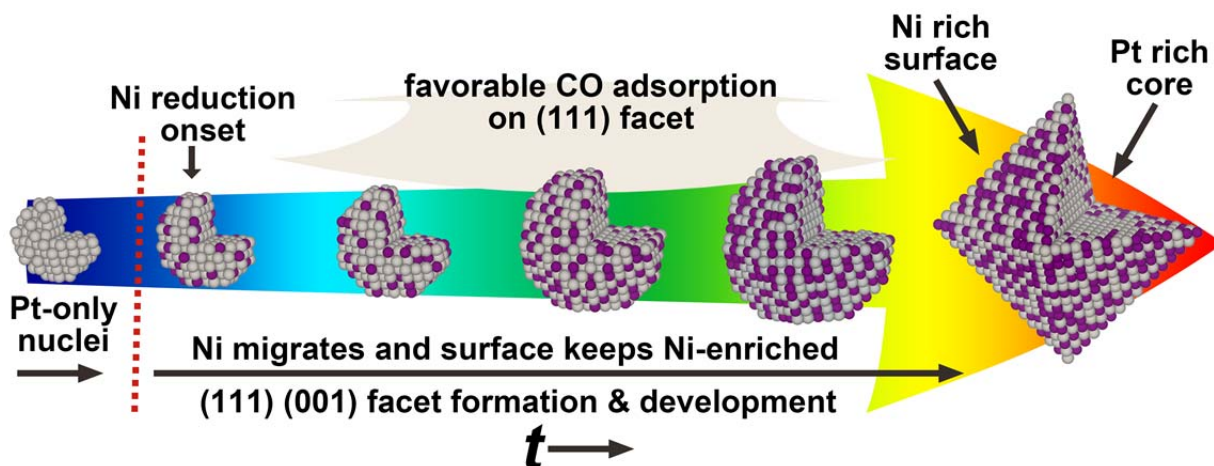
171

172 **Fig. 4.** DFT calculation of CO adsorption energy on the (111) and (001) facets of surface Ni-  
 173 enriched Pt<sub>3</sub>Ni.

174

175 To understand the facet formation mechanism and the possible influences of Ni surface  
 176 segregation on the facet formation, DFT simulations were performed to substantiate our  
 177 conjecture. The results showed that the enrichment of surface Ni significantly enhanced CO  
 178 adsorption on the Pt<sub>3</sub>Ni (111) plane, which led to the formation of an octahedral particle (Fig. 4  
 179 and Table S2). Compared with CO adsorption on Pt (111) ( $E_{\text{ads}} = -1.58$  eV), the adsorption of  
 180 CO molecules was greatly strengthened at both Pt (-1.90 eV) and Ni (-1.82 eV) sites on Ni-  
 181 enriched Pt<sub>3</sub>Ni (111). Although the  $E_{\text{ads}}$  of CO at Pt site (-1.91 eV) on Ni-enriched Pt<sub>3</sub>Ni (001)  
 182 was comparable with that at Pt site on the (111), the value at Ni site on the (001) facet (-1.78 eV)  
 183 was less negative than that at the counterpart Ni site. The  $E_{\text{ads}}$  of CO on Ni-enriched Pt<sub>3</sub>Ni (111)  
 184 was about 0.03 eV more negative than that on the (001) on average. Although the energy  
 185 difference was not dramatic, it altered the favored adsorption facet from the (001) planes for pure  
 186 Pt to the (111) planes for Ni-enriched Pt<sub>3</sub>Ni that contributed to an octahedral morphology  
 187 formation. Noticeably, DFT calculations showed that CO still preferred to adsorb on Pt<sub>3</sub>Ni (001)

188 if there was no Ni enrichment at the surface (fig. S16), which further supported the crucial role  
189 of surface Ni enrichment in Pt<sub>3</sub>Ni for octahedral shape formation.



190  
191 **Fig. 5.** Scheme (not to scale) of octahedral Pt<sub>3</sub>Ni growth pathway with inner section view (gray:  
192 Pt; purple: Ni).

193  
194 A complete picture of the growth mechanism of octahedral Pt<sub>3</sub>Ni can be drawn by considering  
195 all of the information gained from the *in situ* experiments and DFT simulations (Fig.5). Pt nuclei  
196 and spherical clusters generate first under the synthesis condition, which can be attributed to the  
197 stronger reducibility of the Pt precursor. Ni then becomes catalytically reduced by Pt, leading to  
198 a mixed alloy formation. The continued reduction of Pt and Ni results in the growth in particle  
199 size and the evolution of low-index (111) and (001) facets. Along with the particle growth, Ni  
200 segregates outwards induced by CO and enriches the surface. CO molecules adsorb more  
201 preferentially on the Ni-enriched (111) surfaces, which slow down their growth rate. This leads  
202 to the gradual growth of the (111) surfaces and diminishment of the (001), and eventually to the  
203 formation of an octahedral morphology.

204  
205 In conclusion, we combined using multiple cutting-edge *in situ* characterization techniques to  
206 reveal the growth and facet formation pathway of octahedral Pt<sub>3</sub>Ni nanoparticles. Results  
207 indicate the surface enriched Ni plays a significant role in controlling the octahedra development  
208 by mediating the CO adsorption on (111) and (001) facets of Pt<sub>3</sub>Ni nanoparticles. Our findings  
209 highlight the significance of advanced *in situ* techniques in researching catalyst preparation and  
210 morphology control, providing an insightful understanding in synthesizing shaped catalysts.

## 211 212 **Methods**

### 213 Materials

214 Platinum acetylacetonate (Pt(acac)<sub>2</sub>, 97%) and nickel acetylacetonate (Ni(acac)<sub>2</sub>, 95%) were  
215 purchased from Sigma-Aldrich. Carbon black (C, Vulcan® XC-72R) was purchased from Cabot.  
216 Chloroform (CHCl<sub>3</sub>, 99.9%) was purchased from Fisher Scientific.

217

218 Sample preparation

219 The carbon supported Pt(acac)<sub>2</sub> and Ni(acac)<sub>2</sub> sample for *in situ* experiments was prepared  
220 via a dry impregnation method. In a typical procedure, 40 mg Pt(acac)<sub>2</sub> and 17 mg Ni(acac)<sub>2</sub>  
221 were dissolved in 3 mL chloroform, then the solution was added drop wisely onto 80 mg  
222 pretreated XC-72 carbon (300 °C, overnight) under vigorous stirring. After the impregnation, the  
223 mixed sample (20 wt.% Pt loading, Pt : Ni = 3:1, molar ratio) was sealed in a glass vial and ready  
224 for the *in situ* characterizations. For comparison, the carbon supported pure Pt(acac)<sub>2</sub> and pure  
225 Ni(acac)<sub>2</sub> samples were also prepared through the same procedure.

226  
227 *In situ* STEM

228 *In situ* scanning transmission electron microscopy (STEM) study of Pt<sub>3</sub>Ni octahedra growth  
229 was performed on a double Cs-corrected JEOL-JEM 3100-R05 microscope equipped with the  
230 Protochips Atmosphere™ gas cell system. In a typical method, the pre-mixed carbon supported  
231 precursor was dispersed in anhydrous methanol under sonication. Then the suspension was  
232 dropped directly onto a thermal E-chip and dried under the infrared lamp. The thermal E-chip is  
233 equipped with a thin ceramic heating membrane that can be controlled by the Protochips  
234 Atmosphere™ system. After that, a second E-chip window was then placed on top of the thermal  
235 chip in the holder, and this could create a thin gas chamber sealed from the high vacuum of the  
236 TEM column. The sample was situated between two 30-50 nm thick Si<sub>3</sub>N<sub>4</sub> windows of the E-  
237 chips with a 5 μm gap in between. The cross-section scheme of the assembled gas cell is shown  
238 in Fig. S1. The operation accelerating voltage was 300 kV with a small probe current of 20 pA,  
239 and the heating temperature for the gas cell was 200 °C (based on the Protochips calibration)  
240 with high purity H<sub>2</sub>/CO mixture gas (H<sub>2</sub>: 4%, CO: 96%, purity: 99.9995 %) flow at one  
241 atmosphere (760 Torr).

242  
243 *In situ* AP-XPS

244 *In situ* AP-XPS experiments were performed at the 23-ID-2 (CSX-2) beamline of the National  
245 Synchrotron Light Source II (NSLS-II) at Brookhaven National Laboratory. The end-station was  
246 equipped with a differentially pumped hemispherical analyzer (Specs Phoibos 150 NAP), which  
247 was offset by 70° from the incident synchrotron light and 20° from the surface normal of the  
248 sample (Fig. S2). A more detailed description of the beamline and endstation can be found  
249 elsewhere<sup>24</sup>. A photon energy of 1100 eV was used for all experiments. The powder sample was  
250 pressed onto a tantalum foil, which was clipped onto a ceramic button heater. The temperature  
251 was monitored through a type K thermocouple placed underneath the foil. 100 mTorr H<sub>2</sub> and 500  
252 mTorr CO (Matheson, ultra-high purity) were introduced into the measurement chamber using  
253 variable leak valves, and the pressure was monitored using a capacitance manometer. The  
254 collected XPS spectra were calibrated based on the C 1s = 284.5 eV as a reference. The Pt 4f and  
255 Ni 2p peaks were analyzed using a Shirley-type background with XPSpeak 4.1 software.

256  
257 *In situ* XAS

258 X-ray absorption measurements were acquired on the bending magnet beamline of the  
259 Materials Research Collaborative Access Team (MRCAT) at the Advanced Photon Source,  
260 Argonne National Laboratory. Photon energies were selected using a water-cooled, double-  
261 crystal Si(111) monochromator, which was detuned by approximately 50% to reduce harmonic  
262 reflections. Measurements were made in transmission mode, and data points were acquired in  
263 three separate regions (energies relative to the elemental Ni K-edge 8333 eV and Pt L<sub>3</sub>-edge

264 11564 eV): a pre-edge region (-250 to -30 eV, step size = 10 eV, dwell time = 0.25 s), the  
265 XANES region (-30 to +30 eV, step size = 0.5 eV, dwell time = 0.25 s), and the EXAFS region  
266 (to 13 Å<sup>-1</sup>, step size = 0.07 Å<sup>-1</sup>, dwell time = 1s). The ionization chambers were optimized for  
267 the maximum current with linear response (~1010 photons detected/sec) 95% N<sub>2</sub> and 5% Ar in  
268 the incident ion chamber and 40% N<sub>2</sub> and 60% Ar in the transmission detector for both Ni edge  
269 and Pt edge measurement. A Ni or Pt foil spectrum was acquired simultaneously with each  
270 measurement for energy calibration. Samples were treated in a continuous-flow reactor, which  
271 consisted of a quartz tube (1-inch OD, 10-inch length) sealed with Kapton windows by two  
272 Ultra-Torr fittings (Fig. S3). Ball valves were welded to each Ultra-Torr fitting and served as the  
273 gas inlet and outlet. An internal K type thermocouple (Omega) was placed against the sample  
274 holder to monitor temperature.

275 Samples (~ 10 mg) were pressed into a cylindrical sample holder consisting of six wells,  
276 forming a self-supporting wafer. The samples were treated at 160 °C under H<sub>2</sub>/CO gas (2.5% H<sub>2</sub>,  
277 50% CO and 47.5% Ar, ultra-high purity, 1 atm), and the XAS data were collected *in situ*.

278

### 279 XAS data processing

280 Standard procedures for normalization and background subtraction were performed using  
281 Demeter 0.9.25 software package. The edge energy of the X-ray absorption near edge structure  
282 (XANES) spectrum was determined from the inflection point in the leading edge, i.e., the  
283 maximum in the first derivative of the leading edge of the XANES spectrum. The pre-edge  
284 energies were also obtained in the first derivative using the zero-crossing point. The coordination  
285 parameters were obtained by a least square fit in R-space, k<sup>2</sup>-weighted Fourier transformed data  
286 using Artemis<sup>25</sup>.

287

### 288 DFT calculations

289 All density functional theory (DFT) simulations were performed using the Quantum  
290 ESPRESSO package<sup>26</sup>. Structure relaxation and energy calculation were carried out through  
291 Generalized Gradient Approximation (GGA) and the Perdew-Burke-Ernzerhof (PBE) functional  
292 with Projector-Augmented Wave (PAW) sets from PSLibrary 0.3.1<sup>27</sup>. The bulk lattice of Pt and  
293 intermetallic Pt<sub>3</sub>Ni were optimized prior to the cleavage of the (111) and (001) surface. The slab  
294 models were constructed using six-layer p(2 × 2) close-packed surface with a vacuum layer of 20  
295 Å for both (111) and (001) surfaces. For the surface Ni enriched Pt<sub>3</sub>Ni model, we manually  
296 substituted the targeted Pt atoms in the upper three layers of Pt slab models and left the lower  
297 three layers Ni-free while keeping the overall stoichiometric ratio Pt : Ni = 3 : 1. For all the slab  
298 models, the bottom two layers are fixed during the structure relaxation. And for the CO  
299 adsorption, an on-top adsorption site was chosen to make the simulation consistent. We applied a  
300 plane-wave function cutoff of 50 Ry with a charge density cutoff of 500 Ry to initiate the  
301 calculations, and a k-point mesh of 5 × 5 × 1 was used. All the energies were calculated after the  
302 structures were fully relaxed. The adsorption energy for CO was calculated using the equation  
303  $E_{\text{ads}} = E_{\text{system}} - E_{\text{slab}} - E_{\text{CO}}$ . The weighted  $E_{\text{ads}}$  for Pt and Ni co-exist surface was defined as  $E_{\text{ads,w}}$   
304  $= E_{\text{ads,Pt}} \times \theta_{\text{Pt}} + E_{\text{ads,Ni}} \times \theta_{\text{Ni}}$ , where  $\theta_{\text{Pt}}$  and  $\theta_{\text{Ni}}$  are the surface coverage of Pt and Ni atoms in top  
305 layer.

306

307 **References**

- 308 1. Zhang C, Hwang SY, Trout A & Peng Z. Solid-state chemistry-enabled scalable  
309 production of octahedral Pt–Ni alloy electrocatalyst for oxygen reduction reaction. *J. Am.*  
310 *Chem. Soc.* **136**(22), 7805-7808 (2014).
- 311 2. Huang X, Zhao Z, Cao L, Chen Y, Zhu E, Lin Z, *et al.* High-performance transition  
312 metal-doped Pt<sub>3</sub>Ni octahedra for oxygen reduction reaction. *Science* **348**(6240), 1230-  
313 1234 (2015).
- 314 3. Stamenkovic VR, Fowler B, Mun BS, Wang G, Ross PN, Lucas CA, *et al.* Improved  
315 oxygen reduction activity on Pt<sub>3</sub>Ni(111) via increased surface site availability. *Science*  
316 **315**(5811), 493-497 (2007).
- 317 4. Choi S-I, Xie S, Shao M, Odell JH, Lu N, Peng H-C, *et al.* Synthesis and characterization  
318 of 9 nm Pt–Ni octahedra with a record high activity of 3.3 A/mg<sub>Pt</sub> for the oxygen  
319 reduction reaction. *Nano Lett.* **13**(7), 3420-3425 (2013).
- 320 5. Liao H-G, Zhrebetsky D, Xin H, Czarnik C, Ercius P, Elmlund H, *et al.* Facet  
321 development during platinum nanocube growth. *Science* **345**(6199), 916-919 (2014).
- 322 6. Langille MR, Zhang J, Personick ML, Li S & Mirkin CA. Stepwise evolution of spherical  
323 seeds into 20-fold twinned icosahedra. *Science* **337**(6097), 954-957 (2012).
- 324 7. Ievlev AV, Jesse S, Cochell TJ, Unocic RR, Protopopescu VA & Kalinin SV.  
325 Quantitative description of crystal nucleation and growth from in situ liquid scanning  
326 transmission electron microscopy. *ACS Nano* **9**(12), 11784-11791 (2015).
- 327 8. Li Y, Zang L, Jacobs DL, Zhao J, Yue X & Wang C. In situ study on atomic mechanism  
328 of melting and freezing of single bismuth nanoparticles. *Nat. Commun.* **8**, 14462 (2017).
- 329 9. Liao H-G, Niu K & Zheng H. Observation of growth of metal nanoparticles. *Chem.*  
330 *Commun.* **49**(100), 11720-11727 (2013).
- 331 10. Alloyeau D, Dachraoui W, Javed Y, Belkahla H, Wang G, Lecoq H, *et al.* Unravelling  
332 kinetic and thermodynamic effects on the growth of gold nanoplates by liquid  
333 transmission electron microscopy. *Nano Lett.* **15**(4), 2574-2581 (2015).
- 334 11. Zheng H, Smith RK, Jun Y-w, Kisielowski C, Dahmen U & Alivisatos AP. Observation  
335 of single colloidal platinum nanocrystal growth trajectories. *Science* **324**(5932), 1309-  
336 1312 (2009).
- 337 12. Park J, Elmlund H, Ercius P, Yuk JM, Limmer DT, Chen Q, *et al.* 3D structure of  
338 individual nanocrystals in solution by electron microscopy. *Science* **349**(6245), 290-295  
339 (2015).
- 340 13. Wu J, Shan H, Chen W, Gu X, Tao P, Song C, *et al.* In situ environmental TEM in  
341 imaging gas and liquid phase chemical reactions for materials research. *Adv. Mater.*  
342 **28**(44), 9686-9712 (2016).
- 343 14. Taheri ML, Stach EA, Arslan I, Crozier PA, Kabius BC, LaGrange T, *et al.* Current  
344 status and future directions for in situ transmission electron microscopy. *Ultramicroscopy*  
345 **170**(Supplement C), 86-95 (2016).
- 346 15. Shen X, Dai S, Zhang C, Zhang S, Sharkey SM, Graham GW, *et al.* In situ atomic-scale  
347 observation of the two-dimensional Co(OH)<sub>2</sub> transition at atmospheric pressure. *Chem.*  
348 *Mater.* **29**(10), 4572-4579 (2017).
- 349 16. Dai S, Hou Y, Onoue M, Zhang S, Gao W, Yan X, *et al.* Revealing surface elemental  
350 composition and dynamic processes involved in facet-dependent oxidation of Pt<sub>3</sub>Co  
351 nanoparticles via in situ transmission electron microscopy. *Nano Lett.* **17**(8), 4683-4688  
352 (2017).

- 353 17. Xuyen NT, Jeong HK, Kim G, So KP, An KH & Lee YH. Hydrolysis-induced  
354 immobilization of Pt(acac)<sub>2</sub> on polyimide-based carbon nanofiber mat and formation of  
355 Pt nanoparticles. *J. Mater. Chem.* **19**(9), 1283-1288 (2009).
- 356 18. de Souza MO, Mendes FMT, de Souza RF & dos Santos JHZ. XPS characterization of  
357 nickel-acetylacetonate impregnated in NaX and NaY zeolites. *Micropor. Mesopor.*  
358 *Mater.* **69**(3), 217-221 (2004).
- 359 19. Nassr ABAA, Sinev I, Pohl M-M, Grünert W & Bron M. Rapid microwave-assisted  
360 polyol reduction for the preparation of highly active PtNi/CNT electrocatalysts for  
361 methanol oxidation. *ACS Catal.* **4**(8), 2449-2462 (2014).
- 362 20. Cui C, Gan L, Heggen M, Rudi S & Strasser P. Compositional segregation in shaped Pt  
363 alloy nanoparticles and their structural behaviour during electrocatalysis. *Nat. Mater.* **12**,  
364 765 (2013).
- 365 21. Becknell N, Kang Y, Chen C, Resasco J, Kornienko N, Guo J, *et al.* Atomic structure of  
366 Pt<sub>3</sub>Ni nanoframe electrocatalysts by in situ X-ray absorption spectroscopy. *J. Am. Chem.*  
367 *Soc.* **137**(50), 15817-15824 (2015).
- 368 22. Niu Z, Becknell N, Yu Y, Kim D, Chen C, Kornienko N, *et al.* Anisotropic phase  
369 segregation and migration of Pt in nanocrystals en route to nanoframe catalysts. *Nat.*  
370 *Mater.* **15**, 1188 (2016).
- 371 23. Ahmadi M, Cui C, Mistry H, Strasser P & Roldan Cuenya B. Carbon monoxide-induced  
372 stability and atomic segregation phenomena in shape-selected octahedral PtNi  
373 nanoparticles. *ACS Nano* **9**(11), 10686-10694 (2015).
- 374 24. Palomino RM, Stavitski E, Waluyo I, Chen-Wiegart Y-cK, Abeykoon M, Sadowski JT,  
375 *et al.* New in-situ and operando facilities for catalysis science at NSLS-II: The  
376 deployment of real-time, chemical, and structure-sensitive X-ray probes. *Synchrotron*  
377 *Radiat. News* **30**(2), 30-37 (2017).
- 378 25. Ravel B & Newville M. ATHENA, ARTEMIS, HEPHAESTUS: data analysis for X-ray  
379 absorption spectroscopy using IFEFFIT. *J. Synchrotron Rad.* **12**(4), 537-541 (2005).
- 380 26. Paolo G, Stefano B, Nicola B, Matteo C, Roberto C, Carlo C, *et al.* QUANTUM  
381 ESPRESSO: a modular and open-source software project for quantum simulations of  
382 materials. *J. Phys. Condens. Matter* **21**(39), 395502 (2009).
- 383 27. Dal Corso A. Pseudopotentials periodic table: From H to Pu. *Comput. Mater. Sci.*  
384 **95**(Supplement C), 337-350 (2014).

385

## 386 Acknowledgments

387 This work was supported by National Science Foundation (1665265) (Z.P.). S. Z., S. D., G. W.  
388 G., and X. P. acknowledge the National Science Foundation (grant numbers DMR-1506535 and  
389 CBET-1159240). G. Z. and J. T. M. would like to thank the National Science Foundation and the  
390 Center for Innovative and Strategic Transformation of Alkane Resources (CISTAR) for funding  
391 under Cooperative Agreement No. EEC-1647722. Use of the Advanced Photon Source was  
392 supported by the U.S. Department of Energy, Office of Basic Energy Sciences [grant number  
393 DE-AC02-06CH11357]. MRCAT operations, beamline 10-BM, are supported by the Department  
394 of Energy and the MRCAT member institutions. This research used resources of the 23-ID-2  
395 beamline of the National Synchrotron Light Source II, a U.S. Department of Energy (DOE)  
396 Office of Science User Facility operated for the DOE Office of Science by Brookhaven National  
397 Laboratory under Contract No. DE-SC0012704. This research is also partially supported by

398 Laboratory Directed Research and Development (LDRD15-037) program at Brookhaven  
399 National Laboratory.

400

401 **Author contributions**

402 X.S., C.Z., S.Z., S.D., G.W.G and Z.P. performed the *in situ* STEM characterizations. X.S.,  
403 M.G., Y.P., A.H. and I.W. performed the *in situ* AP-XPS experiments. X.S., G.Z. and Y.P.  
404 conducted the *in situ* XAS tests. X.S., C.Z., Y.P. and S.M.S prepared the samples. X.S.  
405 performed the DFT simulations. X.S. analyzed the *in situ* STEM and AP-XPS data. X.S. and  
406 G.Z. analyzed the *in situ* XAS data. X.S. prepared the manuscript and I.W., J.T.M, X.P. and Z.P.  
407 revised the manuscript.

408

409 **Additional information**

410 Supplementary information is available online at [www.nature.com](http://www.nature.com). Reprints and permissions  
411 information is available online at [www.nature.com/reprints](http://www.nature.com/reprints).

412 Correspondence and requests for materials should be addressed to Z.P.

413 **Competing financial interests**

414 The authors declare no competing financial interests.

415

416